**OPEN**

# Some Effects of Different Constitutive Laws on FSI Simulation for the Mitral Valve

Li Cai[1], Ying Wang[1], Hao Gao[2], Xingshuang Ma[3], Guangyu Zhu[4], Ruihang Zhang[1], Xiaoqin Shen[5] & Xiaoyu Luo [6] [2]

In this paper, three different constitutive laws for mitral leaflets and two laws for chordae tendineae are selected to study their effects on mitral valve dynamics with fluid-structure interaction. We first fit these three mitral leaflet constitutive laws and two chordae tendineae laws with experimental data. The fluid-structure interaction is implemented in an immersed boundary framework with finite element extension for solid, that is the hybrid immersed boundary/finite element(IB/FE) method. We specifically compare the fluid-structure results of different constitutive laws since fluid-structure interaction is the physiological loading environment. This allows us to look at the peak jet velocity, the closure regurgitation volume, and the orifice area. Our numerical results show that different constitutive laws can affect mitral valve dynamics, such as the transvalvular flow rate, closure regurgitation and the orifice area, while the differences in fiber strain and stress are insignificant because all leaflet constitutive laws are fitted to the same set of experimental data. In addition, when an exponential constitutive law of chordae tendineae is used, a lower closure regurgitation flow is observed compared to that of a linear material model. In conclusion, combining numerical dynamic simulations and static experimental tests, we are able to identify suitable constitutive laws for dynamic behaviour of mitral leaflets and chordae under physiological conditions.

Because mitral valve (MV) has a very complex tissue structure, any change or loss of its structure will lead to valve diseases. In recent years, valve disease have become one of the major cardiovascular diseases[1]. It is estimated that 850000 patients will be treated with valve replacement by 2050[2]. It is being recognized that the mathematical modelling and numerical simulation of the interaction between MV and blood flow are of great value and significance to deepen our understanding of valve-related diseases and treatment[3–6].

Since early of the 19th century, researchers began to study MV geometric features and have made great progress. Different types of MV model have been developed for simulating MV dynamics, such as symmetrical geometries[7–10], and idealized parametric models[11]. The rapid development of non-invasive clinical imaging technologies, such as ultrasound, computed tomography and magnetic resonance, have allowed the construction of patient-specific MV model. For example, Lim et al.[12] built an asymmetric MV model with three-dimensional (3-D) dynamic boundaries and non-linear pressure loadings over the whole cardiac cycle based on in-vivo experimental data. Wenk et al.[13] developed a finite element (FE) model consisting of the left ventricle, the MV leaflet and chordae tendineae using magnetic resonance images of sheep. Wang et al.[14] reconstructed a patient-specific MV geometry using a multi-slice CT scan with detailed leaflet thickness and chordae tendineae structure. Ma et al.[15] and Gao et al.[16] developed MV models based on magnetic resonance images with fluid-structure interaction (FSI). In a recent study, Toma et al.[17] constructed a MV model based on a sheep $\mu$CT image data.

Early mechanical studies considered MV material as a linear elastic material[18–20] due to its simplicity. However, various mechanical stretching experiments have shown that MV leaflets have characteristics of hyperelasticity and anisotropy[21–26]. May-newman and Yin[27] described the nonlinear mechanical behaviors of porcine MV leaflet, and they demonstrated that the constitutive law could be derived from the hyperelastic framework under the

[1]NPU-UoG International Cooperative Lab for Computation and Application in Cardiology, Northwestern Polytechnical University, Xi'an, 710129, China. [2]School of Mathematics and Statistics, University of Glasgow, Glasgow, G12 8QQ, UK. [3]Bioengineering College, Chongqing University, Chongqing, 400030, China. [4]School of Energy and Power Engineering, Xi'an Jiaotong University, Xi'an, 710049, China. [5]School of Sciences, Xi'an University of Technology, Xi'an, 710048, China. Correspondence and requests for materials should be addressed to Y.W. (email: wangying319@mail.nwpu.edu.cn) or R.Z. (email: ruihangz0313@mail.nwpu.edu.cn)

assumption of material incompressibility and transverse isotropy. Prot et al.[28] proposed two transversely isotropic hyperelastic laws for MV leaflet, and their results showed that their constitutive laws could be used to describe the mechanical properties of the normal and pathological mitral valve. Wang et al.[14] employed a similar constitutive law by considering two family collagen fibers and associated dispersion with parameters estimated from ex vivo experimental data. Gao et al.[16,29] studied MV dynamics using a transverse isotropic strain-invariants law. There are many other forms of constitutive laws for MV leaflets existed in the literature, however, there is no agreement on which law best characterizes MV properties and predicts its dynamics.

Modelling MV dynamics are often based on structure-only models using finite element method (FEM)[12,28,30]. In the structure-only models, the transvalvular pressure load is usually directly applied to the MV leaflets as the boundary conditions. FEM is usually used for numerical implementation to study the normal MV dynamics[7], diseased MV[8,31], the postoperative repair[31,32], etc. n a series of studies. Lee et al.[33,34] have developed a micro- and macro- anatomically accurate MV FE model by incorporating fiber microstructure and interstitial cellular activities to study MV dynamics and facilitate treatment of diseased MV in a multiscale perspective. Besides, there were some FEM models of MV models by Wang[14] and Prot et al.[21,22,28]. For recent reviews, readers are referred to[5,6].

Physiological loading of the MV means that fluid-structure interaction (FSI) is also required to describe the MV dynamics. FSI models of MV have also been developed for decades[16,19,29,35–37] by taking account of not only the MV structure, but also the flow field of the blood. Arbitrary Lagrangian-Eulerian (ALE) method has been most widely used to address FSI problems. For example, Dimasi et al.[38] used in vitro and ALE FSI modeling to simulate the function of a bileaflet mechanical valves in normal and stenotic conditions with symmetric and asymmetric leaflet opening. However, ALE usually requires mesh regeneration to deal with large structural deformation, which would lead to computational difficulties when dealing with the MV dynamics. To overcome such difficulty, immersed boundary (IB) method[39] and fictitious domain method[40] have been developed. For example, Hart et al.[41] and Loon et al.[42] simulated valvular function using the fictitious domain method to analyze the coupling effects of the blood and the valve. Toma et al.[17] studied the chordal forces using an ovine FSI MV system implemented with smoothed particle hydrodynamics, and validated with an advanced in vitro system. Our group has been developing FSI MV models using the IB approach over a decade. Watton et al.[43] used a classical IB method to model a prosthetic bileaflet valve, which agreed well with the numerical results of a commercial software ANSYS. They also studied the effects of left ventricular motion on the MV dynamics[19]. Using an IB method, Luo et al.[44] studied the effects of valve dynamics including the bending stiffness of the valve leaflets and artificial chordae tendineae. Ma et al.[15] used a realistic MV model reconstructed from in vivo magnetic resonance imaging to study MV dynamics. Because soft tissue in general is anisotropic, hyperelastic and nearly incompressible, Boffi et al.[45] developed an immersed boundary method with finite element discretization for the structure part. Griffith and Luo[46] developed a hybrid approach by discretizing the incompressible Navier-Stokes equation by finite difference and the immersed structure by finite element (IB/FE). The advantage of using FE is that hyper-elasticity can be incorporated with experimentally characterized constitutive laws, which can be difficult in classical IB methods in which solid is represented by pseudo fibers[39,44]. By employing the IB/FE approach, Gao et al.[16] simulated MV dynamics using a MV geometry reconstructed from in vivo magnetic resonance images, and further extended to a coupled MV and left ventricle[29]. In a recent study, Liu et al.[47] studied the energy budget in an IB/FE MV model after a careful verification with the commercial FEM software ABAQUS.

Recent experimental or computational studies have found that the chordae tendineae plays an important role in the realization of MV function[17,48–50]. Therefore, it is necessary to incorporate suitable mechanial responses of chordae tendineae into MV models, particularly since most of the studies have used linear material models for chordae tendineae[7,9,10]. There were a few studies on the mechanical properties of the chordae tendineae using uniaxial tensile testing, on leaflet type[51], insertion position[52] or chordal size[53]. These studies showed that the chordae tendineae exhibits nonlinear mechanical properties and the thicker chords (strut chordae) are more extensible with lower modulus than the thinner chords (marginal chordae). However, recent uniaxial experiments with more accurate digital image tracking system from Sun's group[51,54] showed that there was no significant difference in tangent modulus between different kinds of chordae.

Although tensile tests of MV and chordae are important, given that physiological loading condition is dynamic and involves FSI, it is also important to evaluate the mechanical responses using various different constitutive laws with a dynamic mitral FSI system. To our best knowledge, this approach has not been fully exploited. In this study, we aim to compare three different constitutive laws for MV leaflets and two constitutive laws for chordae tendineae using an IB/FE FSI MV model developed earlier[16], and to identify suitable constitutive laws that gives the optimal performance of MV dynamics.
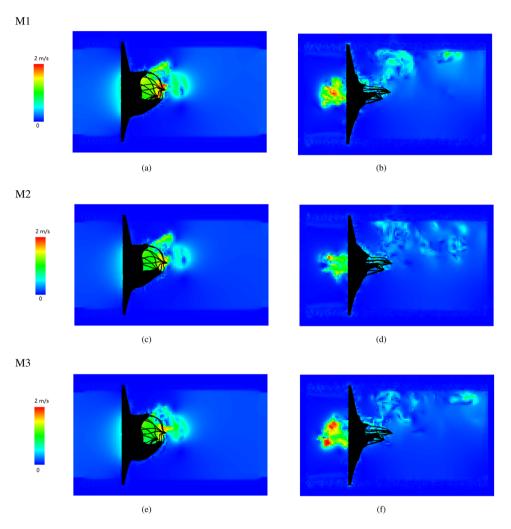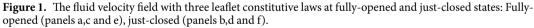
## Results

### The effects of different constitutive laws of MV leaflets.
With the same linear elastic constitutive law of chordae tendineae, cases M1, M2 and M3 are used to describe the mechanical properties of valve leaflets. For all three cases, the MV is fully opened at $t = 0.1\,s$ with a pressure gradient of $10\,mmHg$; at $t = 0.22\,s$, the mitral valve is just closed with a pressure difference of around $80\,mmHg$; and at $t = 0.35\,s$, the MV is fully loaded, the pressure gradient reaches $150\,mmHg$. Table 1 shows the average and maximum displacements with three constitutive laws at fully-opened and fully-loaded states. We can see that there are some differences among the three cases. For example, the average displacement from case M3 is the largest when fully opened, while that of case M1 is the largest when fully loaded. This indicates that different leaflets constitutive laws would affect MV dynamics with FSI.

Figure 1 shows the velocity fields at fully-opened and just-closed states using the three constitutive laws of leaflets, respectively. It can be found that at fully-opened state (Fig. 1(a,c,e)), a strong jet is formed toward the outlet (the left ventricle side). When the MV is just closed (Fig. 1(b,d,f)), the MV leaflets prevent further blood flowing back into the left atrium side with a clear closure regurgitation, especially in cases M1 and M3. Although

| Constitutive law | Average displacement (cm) | | Maximum displacement (cm) | |
|---|---|---|---|---|
| | Fully opened | Fully loaded | Fully opened | Fully loaded |
| M1 | 0.16 ± 0.30 | 0.26 ± 0.37 | 1.21 | 1.59 |
| M2 | 0.14 ± 0.24 | 0.20 ± 0.31 | 1.13 | 1.54 |
| M3 | 0.20 ± 0.36 | 0.25 ± 0.38 | 1.38 | 1.52 |

**Table 1.** The average and maximum displacements.



**Figure 1.** The fluid velocity field with three leaflet constitutive laws at fully-opened and just-closed states: Fully-opened (panels a,c and e), just-closed (panels b,d and f).

the general flow fields in the three cases are similar, there are some minor differences. For example, the jet in case M1 at fully-opened state is stronger than the other two cases, while the closure regurgitation flow is stronger in case M3 than other two cases. The peak jet velocity at different times are given in Table 2. Slightly lower peak velocities can be found in case M2.

Figures 2 and 3 show the fiber strain and stress distributions. When the MV leaflets are fully opened, both the anterior and posterior leaflets are stretched along the fiber direction with low stress due to low diastolic loading. With increased transvalvular pressure, the valve leaflets start to close. When the valve is fully loaded, regions near commissures are highly compressed in cases M1 and M3, but not in case M2. The MV leaflets are further pushed towards the left atrium side with increased pressure, better closer configurations are achieved in cases M1 and M3 with smaller orifice area compared to case M2 at fully-loaded state. When the MV is closed, all cases show high stress concentration near the annulus region, the stress level in case M2 is higher than the other two cases. In order to further analyze fiber strain and stress of leaflets, we define three local regions at the anterior leaflet: two trigones and one belly region, as shown in Fig. 4. The average fiber stress and strain of these regions are summarized in Tables 3 and 4, respectively. When the MV is fully opened, the stress in the belly region is greater than that in the trigone regions; when the MV is just closed, the stress of leaflets begin to increase with much higher

| Constitutive model | Maximum velocity of flow field (m/s) | | |
|---|---|---|---|
| | fully opened | just closed | fully loaded |
| M1 | 2.0 | 2.3 | 0.7 |
| M2 | 2.0 | 1.9 | 0.7 |
| M3 | 2.1 | 2.4 | 0.9 |

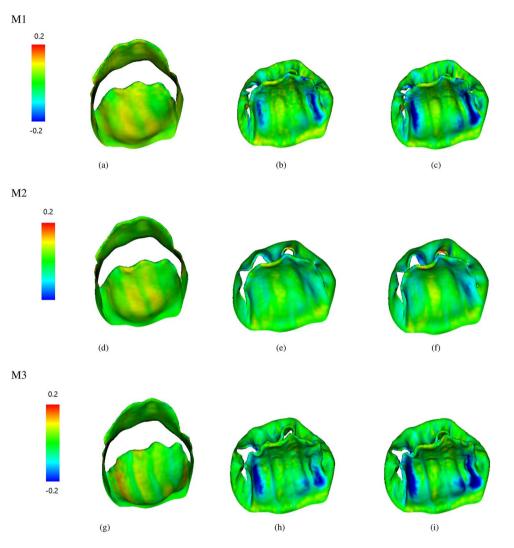**Table 2.** Peak velocity of transvalvular flow.



**Figure 2.** Fiber strain distributions of three constitutive laws of valve leaflet: Fully-opened (panels a,d and g), just-closed (panels b,e and h), and fully-loaded (panels c,f and i).

values in the trigones than that in the belly region; the stresses of the MV continue to increase until the MV is fully loaded. We note that at fully-opened state, all three cases experience similar stress level, while at just-closed and fully-loaded states, case M3 seems experiencing lower stress level compared with other two cases which may be caused by higher level compression in the leaflets (Fig. 2(h)).

The transvalvular flow rates for all three cases are shown in Fig. 5. The flow rate of case M3 is higher than cases M1 and M2 in the diastolic filling phase (before 0.17 s), with M2 the lowest. When the MV begins to close, the flow rate decreases to a negative value when the closure regurgitation occurs. The regurgitation flow rates of cases M1 and M2 are similar, but much larger in case M3. Finally, the MV flow rate gradually returns to zero when the MV is fully closed. The regurgitation flow during MV closure are listed in Table 5. The results are consistent with the values from our previous work[16]. It can be found case M2 has the smallest regurgitation closing flow, while highest in case M3.

We further calculate the orifice area (OA) at fully-opened and just-closed states. In general, the higher the OA, the smaller the energy loss[55]. To calculate OA, the leaflet free-edges are first projected to the annular plane, and then the enclosed area by the project boundaries is considered to be the real OA. Table 6 shows that case M1
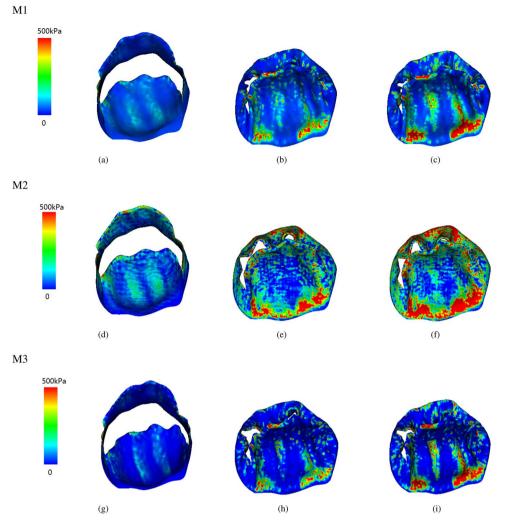
M1



(a)     (b)     (c)

M2



(d)     (e)     (f)

M3



(g)     (h)     (i)

**Figure 3.** Fiber stress distributions of three constitutive laws of valve leaflets: Fully-opened (panels a,d and g), just-closed (panels b,e and h), and fully-loaded (panels c,f and i).
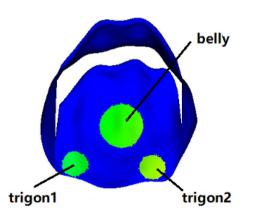


**Figure 4.** Three predefined local regions in the anterior leaflet for stress and strain calculation.

has the largest OA at fully-opened state and smallest OA at just-closed state, which indicates the impedance of case M1 in the diastolic filling is lower compared to other two cases and is closed more tightly in systole. The OA values from the three cases at fully-opened state are also within the interval (4–6 cm$^2$) given by Luo et al.[44].

In summary, of all three models, the constitutive law M2 has the lowest leaflet displacements, lowest peak velocities at fully-opened and closed state, highest fiber stress at fully-loaded state, and lowest OA when fully-opened and the larger OA at closure. The constitutive law M1 achieves largest OA at fully-opened state

| Model | Average stress along fiber direction (kPa) | | | | | | | | |
|---|---|---|---|---|---|---|---|---|---|
| | Fully opened | | | Just closed | | | Fully loaded | | |
| | M1 | M2 | M3 | M1 | M2 | M3 | M1 | M2 | M3 |
| Trigon 1 | 34 | 28 | 6 | 130 | 180 | 89 | 255 | 325 | 238 |
| Trigon 2 | 18 | 18 | 12 | 142 | 213 | 110 | 280 | 439 | 260 |
| The belly region | 52 | 59 | 16 | 78 | 147 | 62 | 127 | 283 | 124 |

**Table 3.** Average stresses along fiber direction on three local regions.

| Model | Average strain along fiber direction | | | | | | | | |
|---|---|---|---|---|---|---|---|---|---|
| | Fully opened | | | Just closed | | | Fully loaded | | |
| | M1 | M2 | M3 | M1 | M2 | M3 | M1 | M2 | M3 |
| Trigon 1 | 0.10 | 0.10 | 0.10 | 0.09 | 0.09 | 0.08 | 0.07 | 0.09 | 0.07 |
| Trigon 2 | 0.10 | 0.10 | 0.10 | 0.09 | 0.10 | 0.08 | 0.08 | 0.09 | 0.07 |
| The belly region | 0.10 | 0.12 | 0.10 | 0.10 | 0.10 | 0.10 | 0.10 | 0.12 | 0.10 |

**Table 4.** Average strains along fiber direction on three local regions.

| | M1 | M2 | M3 |
|---|---|---|---|
| Regurgitation flow | 11.5741 | 8.7164 | 13.2082 |

**Table 5.** Regurgitation flow (mL) during MV closure.

| | M1 | M2 | M3 |
|---|---|---|---|
| fully-opened | 4.956 | 4.810 | 4.828 |
| just-closed | 0.953 | 1.132 | 1.341 |

**Table 6.** Orifice area ($cm^2$) at different times.



**Figure 5.** Flow rates with three material models for MV leaflets.

and lowest OA at fully-closed state, and smaller regurgitation closure flow. Therefore, the constitutive law M1 is deemed more suitable for predicting MV dynamics with FSI. In the next section, we will use the constitutive law M1 for MV leaflets to study the effects of two different material models of the chordae tendineae on MV dynamics.

**The effects of different constitutive models of the chordae tendineae.** Table 7 gives the displacements with different chordae constitutive laws. The average displacements are almost the same at fully-opened and fully-loaded states, while the maximum displacement from the linear model is slightly larger than that of the exponential model at fully-opened and -closed states.

| Type of chordae tendineae constitutive law | Average displacement (cm) | | Maximum displacement (cm) | |
|---|---|---|---|---|
| | Fully opened | Fully loaded | Fully opened | Fully loaded |
| Liner law | 0.16 ± 0.30 | 0.26 ± 0.37 | 1.21 | 1.59 |
| Exponential law | 0.16 ± 0.29 | 0.25 ± 0.38 | 1.14 | 1.57 |

**Table 7.** Average and maximum displacements from two chordae tendineae models.

| Model | Average strain and stress along fiber direction | | | | | |
|---|---|---|---|---|---|---|
| | t = 0.1 s | | t = 0.22 s | | t = 0.35 s | |
| | Strain | Stress (kPa) | Strain | Stress (kPa) | Strain | Stress (kPa) |
| Trigon 1 | 0.10 | 39 | 0.09 | 116 | 0.07 | 241 |
| Trigon 2 | 0.09 | 36 | 0.09 | 147 | 0.08 | 282 |
| The belly region | 0.10 | 54 | 0.10 | 74 | 0.10 | 130 |

**Table 8.** Average strain and stress along fiber direction on the three local regions using an exponential model for the chordae tendineae.
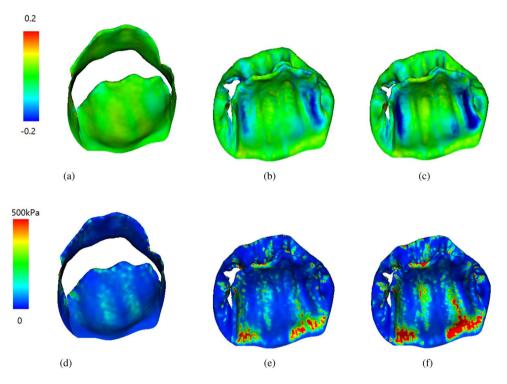


**Figure 6.** Strain and stress distributions with an exponential constitutive law of the chordae tendineae. Fully-opened (panels a and d), just-closed (panels b and e), and fully-loaded (panels c and f).

We summarize the fiber stress and strain results of the exponential model in Fig. 6. Comparing with the case M1 of Figs 2 and 3, we find that the stress and strain distributions of the two chordae tendineae constitutive laws are also similar. The average stress and strain of defined three regions for the exponential constitutive law are shown in Table 8. Compared to the results for the linear model (case M1), the stress level of the exponential model is slightly higher than that of the linear model. Figure 7 shows the flow rates through the MV, although slightly higher flow rate can be achieved in the linear model during diastolic filling phase (before 0.17 s), larger regurgitation closure flow exists compared to the exponential law, suggesting that the MV closes tighter when an exponential law is chosen for chordae tendineae.
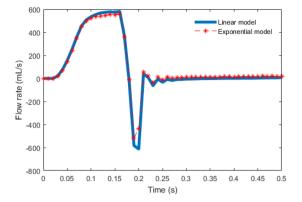
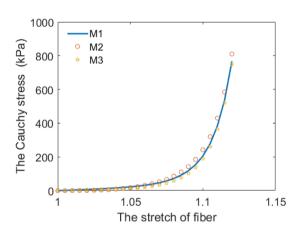**Figure 7.** The comparison of the flow rates with chordae tendineae constitutive laws.



**Figure 8.** The stretch-stress relationships for the anterior leaflet along fiber direction.
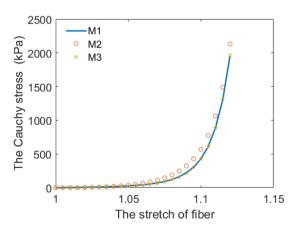


**Figure 9.** The stretch-stress relationships for the posterior leaflet along fiber direction.

## Discussion

In this paper, we use the IB/FE method to study the effects of different constitutive laws on MV dynamics with fluid-structure interaction. We select three different constitutive laws of MV leaflets and two material models for chordae tendineae. Parameters of different constitutive laws of leaflets are determined by matching the biaxial stretch-stress relationship along the fiber direction and the cross-fiber direction with stretch-stress relationships derived from the constitutive law M1[16]. The fitted stretch-stress curves are shown in Figs 8–9. Constitutive parameters for chordae tendineae are determined by fitting uniaxial stretching experiments of porcine chordae tendineae. All constitutive laws can capture the mechanical behavior of the MV with R-squared values similar, so then we compare the MV dynamic behaviors with different constitutive laws of the leaflet and chordae tendineae. Results show that case M1 has the largest OA at fully-opened state and the smallest OA at just-closed state, the
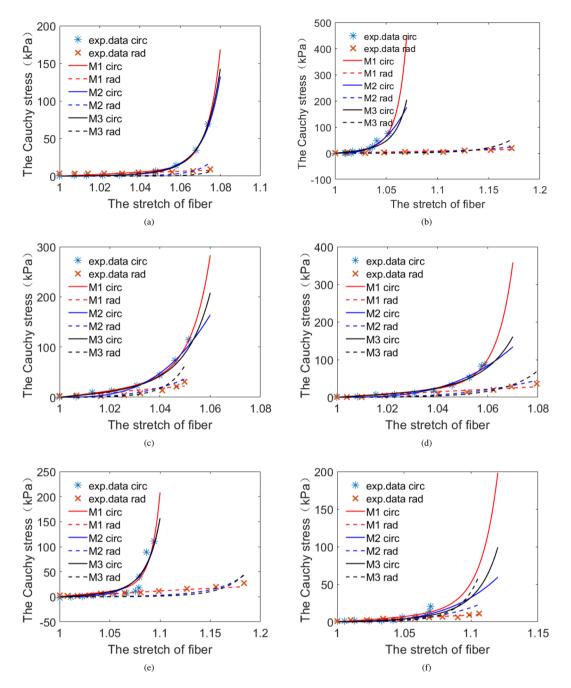
**Figure 10.** Fitting the three constitutive laws (Eq. 9) to our own bi-axial porcine experimental data for the anterior leaflet (panels a,c and e) and the posterior leaflet (panels b,d and f). Case 1 (panels a and b), Case 2 (panels c and d), Case 3 (panels e and f).

regurgitation closing flow of case M1 and the exponential chordae tendineae model are lower than others. Our results may suggest that the combination of M1 constitutive law for the leaflet and the exponential law for chordae tendineae would be more suitable for simulating MV dynamics with FSI.

Through *in vitro*[24,25,56] and *in vivo*[57] studies, many researchers have also studied the mechanical properties of MV by uniaxial and biaxial stretching experiments[23,51], and those experimental data have shown that valve leaflets and chordae tendineae have the characteristics of anisotropy and non-linearity. In papers[37,58–60], linear elastic valve material models were used, which was impractical. Therefore, we choose fiber-reinforced constitutive laws for the MV leaflet[22,23] in this study, a common practice in current soft tissue modelling. We further find that the three selected MV leaflets constitutive laws can fit to our own porcine MV experiments very well, as shown in Fig. 10.

The strain and stress distributions along fiber direction at different time are shown in Figs 2, 3 and 6. It can be seen that for different constitutive laws, most of the leaflets regions are tensile along the fiber direction and some of regions are compressed at closed state, which is, in general, consistent with the results of the papers[22,23].

Detailed strain and stress analysis in three regions are given in Tables 3–4 and 8. In the paper[43], the maximum fiber strain is 0.4, which is larger than our results. However, our model prediction of the circumferential stresses range seems to agree well with the measurements from *in vivo* measurements[25,61]. For example, the circumferential stresses[25,61] of valve leaflets range from 200 to 280 kPa at fully-loaded state. There are some differences among different constitutive laws for MV leaflets. For example, case M2 exhibits a greater stress on the posterior valves, while cases M1 and M3 experience almost the same stress level. In addition, we find that the stresses are mainly concentrated on the annulus ring and the edge of the MV leaflets during closure. When the exponential constitutive law of the chordae tendineae is used to replace the linear constitutive law, we find that the strain level of MV leaflets is larger than that of the linear model, but still within the ranges reported in[62].

Additionally, we have compared several quantities to evaluate three different material models of MV leaflets, including the peak jet velocity, the closure regurgitation volume and the orifice area. The difference in peak velocity is minor for the three cases according to Table 2. As for the amount of regurgitation flow, case M2 has the lowest regurgitant volume and M3 has the highest regurgitant volume. Table 6 shows that case M1 has the biggest orifice area when fully opened and the smallest when just closed. The orifice area values at fully-opened state are within the interval (4–6 cm$^2$) reported[44].

## Methods

### IB/FE method.

The IB/FE method developed by Griffith and Luo[46] is employed to simulate MV dynamics in this study. The governing equations of the FSI system are

$$\rho\left(\frac{\partial \mathbf{u}}{\partial t}(\mathbf{x}, t) + \mathbf{u}(\mathbf{x}, t) \cdot \nabla \mathbf{u}(\mathbf{x}, t)\right) = -\nabla p(\mathbf{x}, t) + \mu \nabla^2 \mathbf{u}(\mathbf{x}, t) + \mathbf{f}^e(\mathbf{x}, t),$$ (1)

$$\nabla \cdot \mathbf{u}(\mathbf{x}, t) = 0,$$ (2)

$$\mathbf{f}^e(\mathbf{x}, t) = \int_E \mathbf{F}^e(\mathbf{X}, t)\delta(\mathbf{x} - \chi(\mathbf{X}, t))d\mathbf{X},$$ (3)

$$\frac{\partial \chi(\mathbf{X}, t)}{\partial t} = \int_\Omega \mathbf{u}(\mathbf{x}, t)\delta(\mathbf{x} - \chi(\mathbf{X}, t))d\mathbf{x},$$ (4)

$$\int_E \mathbf{F}(\mathbf{X}, t) \cdot \mathbf{V}(\mathbf{X})d\mathbf{X} = -\int_E \mathbf{P}^e : \nabla \mathbf{V}(\mathbf{X})d\mathbf{X}.$$ (5)

where $\mathbf{X} = (X_1, X_2, X_3) \in E$ denotes the material (Lagrangian) coordinates in the reference configuration, $\mathbf{x} = (x_1, x_2, x_3) \in \Omega$ denotes the Cartesian (Eulerian) coordinates. $\Omega \subset R^3$ denotes the physical region occupied by the fluid-structure system, and $E \subset R^3$ denotes the region occupied by the immersed structure (such as the mitral valve, chordae tendineae, etc) in the reference configuration. $\rho$ is the fluid density, $p(\mathbf{x}, t)$ is the Eulerian pressure, and $\mu$ is the viscosity. $\chi(\mathbf{X}, t) \in \Omega$ gives the physical position of material point $\mathbf{X}$ at time $t$. Therefore, the physical region occupied by the structure at time $t$ is $\Omega^e(t) = \chi(E, t)$, and the physical domain occupied by the fluid at time $t$ is $\Omega^f(t) = \Omega - \Omega^e(t)$. A three-dimensional regularised delta function $\delta(\mathbf{x}) = \delta(x_1)\delta(x_2)\delta(x_3)$ was used to describe the fluid-structure interaction, which implies that the IB/FE approach permits nonconforming discretization of the fluid and structure domains. $\mathbf{P}^e = \frac{\partial \Psi}{\partial \mathbf{F}}$ is the first Piola-Kirchhoff (PK) stress tensor, which is calculated from a strain-invariant based strain energy function $\Psi$.

The total Cauchy stress tensor of the coupled fluid-structure system is

$$\sigma(\mathbf{x}, t) = \sigma^f(\mathbf{x}, t) + \begin{cases} \sigma^e(\mathbf{x}, t) & \text{for } \mathbf{x} \in \Omega^e \\ 0 & \text{otherwise} \end{cases}$$ (6)

where $\sigma^f = -p(\mathbf{x}, t)\mathbf{I} + \mu[\nabla \mathbf{u}(\mathbf{x}, t) + (\nabla \mathbf{u}(\mathbf{x}, t))^T]$ is the fluid-like stress tensor. $\mathbf{I}$ is the identity matrix, and $\sigma^e$ is the elastic stress tensor, defined as

$$\sigma^e = \begin{cases} J^{-1}\mathbf{P}^e\mathbf{F}^T & \text{for } \mathbf{x} \in \Omega^e \\ 0 & \text{otherwise} \end{cases}$$ (7)

where $\mathbf{F} = \frac{\partial \chi}{\partial \mathbf{X}}$ is the deformation gradient and $J = \det(\mathbf{F})$.

### Constitutive laws and parameters.

Biological tissues usually can be modeled as nonlinear elastic materials, and their material parameters could be obtained from uniaxial or biaxial tensile testing, in which tissue samples are subjected to various stretching configurations along different directions. MV anatomy experiments show that valve tissue is basically composed of fibrous tissue[51,63], mainly collagen and elastin, and the liquid (mainly water). At low strain, the wavy structure can be extended by relatively low stress, but with the increase of strain, the fiber straightens gradually and the overall response of the structure becomes more rigid. To determine material parameters, an inverse problem is usually formulated by minimizing the differences between the predicted stretch-stress data derived from selected constitutive laws and experimentally measured data, that is

| Parameters | $c$(kPa) | $a$(kPa) | $b$ |
|---|---|---|---|
| Anterior leaflet | 17.4 | 31.3 | 55.93 |
| Posterior leaflet | 10.2 | 50.0 | 63.48 |

**Table 9.** The constitutive parameters of M1.

| Parameters of M2 | $\bar{c}_0$(kPa) | $\bar{c}_1$(kPa) | $\bar{c}_2$ | Average error |
|---|---|---|---|---|
| Anterior leaflet | 7.69 | 69.42 | 0.0008 | 15.0 |
| Posterior leaflet | 13.99 | 80.22 | 0.1447 | 57.1 |
| **Parameters of M3** | $c_0$(kPa) | $c_1$(kPa) | $c_2$ | **Average error** |
| Anterior leaflet | 0.29 | 0.47 | 55.39 | 10.4 |
| Posterior leaflet | 0.44 | 2.58 | 61.46 | 3.6 |

**Table 10.** The constitutive parameters of M2 and M3.

$$\arg\min_{c_1,c_2,c_3,\cdots} \quad \sum[(\sigma_{11}^{\text{model}} - \sigma_{11}^{\text{exp}})^2 + (\sigma_{22}^{\text{model}} - \sigma_{22}^{\text{exp}})^2 + \cdots]$$
$$c_i > g_i \tag{8}$$

where $c_i$ ($i \geq 1$) are non-negative material parameters and $g_i$ are constraints of constitutive constants, i.e. >0, and $\sigma^{\text{model}}$ is calculated from some constitutive laws, $\sigma^{\text{exp}}$ are experimental measurements.

**The constitutive laws of the mitral valve leaflets.** In this study, three fiber-reinforced strain energy functions (cases M1, M2 and M3, Eq. 9) are chosen to characterize the mechanical responses of MV leaflets, all are based on strain invariants of $I_1$ and $I_4$, respectively, and

$$I_1 = \text{tr}\mathbf{C}, \quad I_4 = \mathbf{a}_0 \cdot (\mathbf{Ca}_0),$$

in which $\mathbf{C} = \mathbf{F}^T\mathbf{F}$ is the Cauchy-Green deformation tensor, $\mathbf{a}_0$ is the collagen fiber direction at reference state, which is an unit vector. $I_1$ represents the overall deformation, usually is used to describe the isotropic matrix property, and $I_4$ is the squared stretch along the collagen fiber direction.

$$\text{M1: } \Psi(I_1, I_4) = c(I_1 - 3) + \frac{a}{2b}(\exp[b(I_4 - 1)^2] - 1),$$
$$\text{M2: } \Psi(I_1, I_4) = \bar{c}_0(\exp[\bar{c}_1(I_1 - 3)^2 + \bar{c}_2(\sqrt{I_4} - 1)^4] - 1),$$
$$\text{M3: } \Psi(I_1, I_4) = c_0(\exp[c_1(I_1 - 3)^2 + c_2(I_4 - 1)^2] - 1), \tag{9}$$

where $c$, $a$, $b$, $\bar{c}_0$, $\bar{c}_1$, $\bar{c}_2$ and $c_0$, $c_1$, $c_2$ are the non-negative material parameters. We assume collagen fibers can only bear the load when they are stretched, but not in compression, thus $I_4$ in Eq. 9 are replaced by $I_4^* = \max(I_4, 1)$. These three constitutive laws of the valve leaflets are all transversely isotropic materials, case M1 was used in paper[16], case M2 was used in paper[21], and case M3 was from the papers[22,28].

The corresponding Cauchy-stress tensor for the three selected strain energy functions are

$$\sigma^{\text{M1}} = -\lambda\mathbf{I} + 2\mathbf{F}\frac{\partial\Psi}{\partial\mathbf{C}}\mathbf{F}^T$$
$$= -\lambda\mathbf{I} + 2c\mathbf{B} + 2a(I_4)\exp^{b(I_4-1)^2} \cdot \mathbf{Fa}_0 \otimes \mathbf{Fa}_0,$$
$$\sigma^{\text{M2}} = -\lambda\mathbf{I} + 2\mathbf{F}\frac{\partial\Psi}{\partial\mathbf{C}}\mathbf{F}^T$$
$$= -\lambda\mathbf{I} + 4\bar{c}_0\exp[\bar{c}_1(I_1 - 3)^2 + \bar{c}_2(\sqrt{I_4} - 1)^4][\bar{c}_1(I_1 - 3)\mathbf{B} + \bar{c}_2(\sqrt{I_4} - 1)^3\frac{1}{\sqrt{I_4}} \cdot \mathbf{Fa}_0 \otimes \mathbf{Fa}_0],$$
$$\sigma^{\text{M3}} = -\lambda\mathbf{I} + 2\mathbf{F}\frac{\partial\Psi}{\partial\mathbf{C}}\mathbf{F}^T$$
$$= -\lambda\mathbf{I} + 4c_0\exp[c_1(I_1 - 3)^2 + c_2(I_4 - 1)^2][c_1(I_1 - 3)\mathbf{B} + c_2(I_4 - 1) \cdot \mathbf{Fa}_0 \otimes \mathbf{Fa}_0], \tag{10}$$

in which $\lambda$ is a Lagrangian multiplier to enforce the incompressibility, and $\mathbf{B} = \mathbf{FF}^T$.

Parameters for the strain energy function M1 are from Gao et al.[16], which are derived from the *in vitro* testing on a healthy human MV carried out by Wang et al.[64]. The parameters of case M1 are shown in the Table 9. Parameters in cases M2 and M3 are determined by using a "pseudo" biaxial stretching experiments along fiber and cross-fiber directions using case M1. The *fmincon* function in MATLAB is employed to determine the parameters of constitutive laws M2 and M3 by using the Cauchy stress formulas (Eq. 10) by minimizing Eq. 8. The fitted stretch-stress curves for all three laws are given in Figs 8–9, and the estimated parameters of cases M2 and M3 are listed in Table 10, including the average errors.

We further fit the three constitutive laws from Eq. 9 to an *in vitro* biaxial stretching experiment on porcine MV samples. In brief, fresh porcine MV samples were harvested from a local abattoir. Specimens of MV and

| Anterior leaflet | R-squared = 1 − SSE/SST | | |
|---|---|---|---|
| | M1 | M2 | M3 |
| Case1 | 0.9904 | 0.9734 | 0.9532 |
| Case2 | 0.9810 | 0.9822 | 0.9929 |
| Case3 | 0.8987 | 0.9056 | 0.8909 |
| Average value | 0.9567 | 0.9537 | 0.9457 |

**Table 11.** R-squared values of fitting the anterior leaflet with three constitutive laws in Eq. 9 to our porcine MV experiments. SSE is the residual sum of squares, SST denotes the total sum of squares.

| Posterior leaflet | R-squared = 1 − SSE/SST | | |
|---|---|---|---|
| | M1 | M2 | M3 |
| Case1 | 0.9472 | 0.9799 | 0.9561 |
| Case2 | 0.9722 | 0.9822 | 0.9707 |
| Case3 | 0.7742 | 0.8112 | 0.8122 |
| Average value | 0.8979 | 0.9244 | 0.9130 |

**Table 12.** R-squared values of fitting the posterior leaflet with three constitutive laws in Eq. 9 to our porcine MV experiments. SSE is the residual sum of squares, SST denotes the total sum of squares.



**Figure 11.** The fitted stretch-stress relationships for the chordae tendineae.

chordae were then dissected and stored in 4 °C phosphate buffer saline (PBS) before test and submerged in 37 °C PBS bath during test. Planar biaxial tensile test was conducted with a CellScale BioTester (Waterloo, ON, Canada) with 10 N load-cell on MV samples, while uniaxial tensile test (Instron Industrial Products, US) was carried out on chordae samples. The tissue specimens were stretched and released for 8 complete cycles for preconditioning until the load-displacement curve was visibly repeatable. Finally, the MV and chordae specimens were stretched to 1500 mN and 5 N to cover the physiological condition, respectively. The displacement and tensile forces were recorded and used for stress and strain analysis. The thickness of specimens was measured by a digital caliper ($\pm0.01$ mm) three times on random location before the test. We find that all three constitutive laws can fit the experimental data very well as can be seen from Fig. 10, among which cases 1, 2 and 3 represent the three sets of MV data from three hearts. The model M2 shows the best fitting although the difference is small. Corresponding R-squared values are reported in Tables 11–12, all have minor differences for the anterior and posterior leaflet respectively, which suggests that these selected three constitutive laws are suitable for characterizing MV leaflets properties. Thus, we will mainly compare their effects on the MV dynamics using a FSI solver in this study.

**The constitutive laws of the chordae tendineae.** Two constitutive laws are chosen for the chordae tendineae, one is the neo-hooken material model[16], and the second one is the exponential model[28], they are

$$\begin{aligned}\Psi &= C(I_1 - 3),\\ \Psi &= a_1(\exp[a_2(I_1 - 3)] - 1).\end{aligned} \quad (11)$$

in which $C$, $a_1$, and $a_2$ are material constants. The Cauchy stress for the two chordae constitutive laws are

$$\begin{aligned}\sigma &= -\lambda\mathbf{I} + C\mathbf{B},\\ \sigma &= -\lambda\mathbf{I} + 2a_1\exp[a_2(I_1 - 3)]\mathbf{B}.\end{aligned} \quad (12)$$
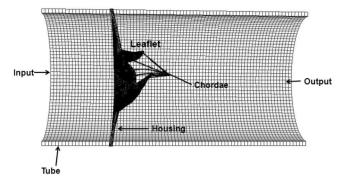
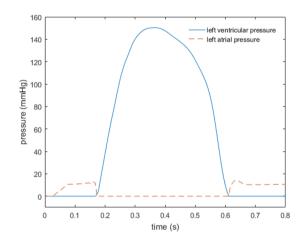**Figure 12.** The IB/FE MV model.



**Figure 13.** Typical human pressure profiles of MV.

Figure 11 shows the fitted stretch-stress curves with the two chordae constitutive laws to our own uniaxial tensile testing experimental data from Dr. Ma's Lab using porcine MV chordae tendineae. It can be found that nonlinear mechanical property of the chordae tendineae can only be better represented by the exponential law.

**The MV model and boundary conditions.**  The MV model is reconstructed from a cardiac magnetic resonance (CMR) imaging of a healthy volunteer, and the leaflets are reconstructed at mid-diastole, and a pseudo-chordae structure is used because the CMR imaging cannot describe the chordal structure *in vivo* due to resolution limitation. Details of the MV geometry reconstruction can be found in our previous study[16,36]. Figure 12 shows the MV with the chordae tendineae, mounted in a housing and then attached to a straight tube (length: 16 cm, radius: 3.8 cm), and immersed into a fluid domain with size 10 cm × 10 cm × 16 cm, which is discretized into 80 × 80 × 128 regular grids.

An explicit version of Crank Nicolson-Adams Backward scheme is used for time stepping, which requires a relatively small time step size ($10^{-5}$ s). The IB/FE MV model is implemented within the open-source IBAMR software framework (https://github.com/IBAMR/IBAMR). The boundary conditions are the same as in paper[16], in brief, pressure boundary conditions are applied to the inlet of the straight tube, pressure profile is shown in Fig. 13. Zero pressure boundary conditions are applied along the rest of the boundaries of the whole computational domain. The housing and the straight tube are fixed in place. CMR measured displacements of the papillary muscles are applied to the chordae attachment points where the chordae tendineae connects the papillary muscles. Further details of the MV model implementation can be found in[16].

**Limitations.**  Finally, we mention the limitations of this study. Though we have incorporated FSI and nonlinear constitutive laws for valve leaflets and chordae tendineae. We have ignored the valve-heart interactions, which will have some impact on the dynamic loading conditions[29]. In addition, our geometric structure is based on a simplified model of chordae tendineae, whereas the realistic chordae tendineae consists of marginal, strut and basal chordae tendineae[17]. We leave investigation of these effects to future research.

## References
1. Baumgartner, H. *et al.* 2017 ESC/EACTS Guidelines for the management of valvular heart disease. *Eur. Hear. J.* **38**, 2739–2791 (2017).
2. Bax, J. J. & Delgado, V. Bioprosthetic heart valves, thrombosis, anticoagulation, and imaging surveillance. *JACC: Cardiovasc. Interv.* **10**, 388–390 (2017).

3. Fried, H. M. Computational modeling of cardiac valve function and intervention. *Annu. review biomedical engineering* **16**, 53 (2014).
4. Sun, W., Martin, C. & Pham, T. Computational modeling of cardiac valve function and intervention. *Annu. review biomedical engineering* **16**, 53–76 (2014).
5. Sacks, M. S. *et al.* On the simulation of mitral valve function in health, disease, and treatment. *J. biomechanical engineering* **141**, 070804 (2019).
6. Gao, H. *et al.* Modelling mitral valvular dynamics-current trend and future directions. *Int. J. for Numer. Methods Biomed. Eng.* **33**, e2858 (2017).
7. Kunzelman, K. S. *et al.* Finite element analysis of the mitral valve. *J. Hear. Valve Dis.* **2**, 326–340 (1993).
8. Kunzelman, K. S., Reimink, M. S. & Cochran, R. P. Annular dilatation increases stress in the mitral valve and delays coaptation: a finite element computer model 1. *Cardiovasc. Surg.* **5**, 427–434 (1997).
9. Lau, K. D., Diaz, V., Scambler, P. & Burriesci, G. Mitral valve dynamics in structural and fluid structure interaction models. *Med. Eng. & Phys.* **32**, 1057–1064 (2010).
10. Zhong, Q., Zeng, W. H., Huang, X. Y. & Wang, B. L. Numerical modeling and biomechanical analysis of the human mitral valve. *J. Med. Biomech* **29**, 53–59 (2014).
11. Shen, X. Q., Wang, T., Cao, X. & Cai, L. The geometric model of the human mitral valve. *Plos One* **12**, e0183362 (2017).
12. Lim, K. H., Yeo, J. H. & Duran, C. M. Three-dimensional asymmetrical modeling of the mitral valve: a finite element study with dynamic boundaries. *J. Hear. Valve Dis.* **14**, 386–392 (2005).
13. Wenk, J. F. *et al.* First finite element model of the left ventricle with mitral valve: insights into ischemic mitral regurgitation. *Annals of Thorac. Surg.* **89**, 1546–1553 (2010).
14. Wang, Q., Sirois, E. & Sun, W. Patient-specific modeling of biomechanical interaction in transcatheter aortic valve deployment. *J. Biomech.* **45**, 1965–1971 (2012).
15. Ma, X., Gao, H., Griffith, B. E., Berry, C. & Luo, X. Image-based fluid structure interaction model of the human mitral valve. *Comput. & Fluids* **71**, 417–425 (2013).
16. Gao, H. *et al.* A finite strain nonlinear human mitral valve model with fluid-structure interaction. *Int. J. for Numer. Methods Biomed. Eng.* **30**, 1597–1613 (2014).
17. Toma, M. *et al.* Fluid-structure interaction analysis of papillary muscle forces using a comprehensive mitral valve model with 3d chordal structure. *Annals Biomed. Eng.* **44**, 942–953 (2016).
18. Salgo, I. S. *et al.* Effect of annular shape on leaflet curvature in reducing mitral leaflet stress. *Circ.* **106**, 711–717 (2002).
19. Watton, P. N., Luo, X. Y., Yin, M., Bernacca, G. M. & Wheatley, D. J. Effect of ventricle motion on the dynamic behaviour of chorded mitral valves. *J. Fluids Struct.* **24**, 58–74 (2008).
20. Finite Element Modeling and Biomechanical Analysis of Mitral Valve. Ph.D. thesis, Xiamen University (2014).
21. Prot, V. & Skallerud, B. An improved transverse isotropic hyperelastic material model for simulation of mitral valve response. *J. Biomech.* **39**, S618–S618 (2006).
22. Prot, V. & Skallerud, B. Nonlinear solid finite element analysis of mitral valves with heterogeneous leaflet layers. *Comput. Mech.* **43**, 353–368 (2009).
23. Prot, V., Skallerud, B., Sommer, G. & Holzapfel, G. A. On modelling and analysis of healthy and pathological human mitral valves: Two case studies. *J. Mech. Behav. Biomed. Mater.* **3**, 167–177 (2010).
24. May-Newman, K. & Yin, F. C. Biaxial mechanical behavior of excised porcine mitral valve leaflets. *Am J Physiol* **269**, 1319–27 (1995).
25. Sacks, M. S. Incorporation of experimentally-derived fiber orientation into a structural constitutive model for planar collagenous tissues. *J Biomech Eng* **125**, 280–287 (2003).
26. Rabbah, J. P. M., Neelakantan, S., Siefert, A. W., Arvind, S. & Yoganathan, A. P. Mechanics of healthy and functionally diseased mitral valves: a critical review. *J. biomechanical engineering* **135**, 021007 (2013).
27. May-Newman, K. & Yin, F. C. A constitutive law for mitral valve tissue. *J. biomechanical engineering* **120**, 38 (1998).
28. Prot, V., Haaverstad, R. & Skallerud, B. Finite element analysis of the mitral apparatus: annulus shape effect and chordal force distribution. *Biomech Model Mechanobiol* **8**, 43–55 (2009).
29. Gao, H. *et al.* A coupled mitral valve-left ventricle model with fluid-structure interaction. *Med. Eng. & Phys.* **47**, 128–136 (2017).
30. Liao, K., Wu, J. J. & Frater, R. W. Intraoperative epicardial echo/doppler evaluation of a stentless, chordally supported quadricusp mitral bioprosthesis. *Asaio J.* **39**, M634 (1993).
31. Kunzelman, K. S., Quick, D. W. & Cochran, R. P. Altered collagen concentration in mitral valve leaflets: biochemical and finite element analysis. *Annals Thorac. Surg.* **66**, S198 (1998).
32. Kunzelman, K. S., Reimink, M. S. & Cochran, R. P. Flexible versus rigid ring annuloplasty for mitral valve annular dilatation: a finite element model. *J. Hear. Valve Dis.* **7**, 108–116 (1998).
33. Lee, C.-H. *et al.* On the effects of leaflet microstructure and constitutive model on the closing behavior of the mitral valve. *Biomech. Model. Mechanobiol.* **14**, 1281–1302 (2015).
34. Lee, C.-H. *et al.* On the *in vivo* function of the mitral heart valve leaflet: insights into tissue–interstitial cell biomechanical coupling. *Biomech. Model. Mechanobiol.* **16**, 1613–1632 (2017).
35. Kunzelman, K. S., Einstein, D. R. & Cochran, R. P. Fluid-structure interaction models of the mitral valve: function in normal and pathological states. *Philos. Transactions Royal Soc. Lond.* **362**, 1393–1406 (2007).
36. Ma, X. S., Gao, H., Griffith, B. E., Berry, C. & Luo, X. Y. Image-based fluid-structure interaction model of the human mitral valve. *Comput. & Fluids* **71**, 417–425 (2013).
37. Lee, C. H., Rouzbeh, A., Gorman, R. C., Gorman, J. H. & Sacks, M. S. An inverse modeling approach for stress estimation in mitral valve anterior leaflet valvuloplasty for *in-vivo* valvular biomaterial assessment. *J. Biomech.* **47**, 2055–2063 (2014).
38. Dimasi, A. *et al.* Fluid-structure interaction and *in vitro* analysis of a real bileaflet mitral prosthetic valve to gain insight into doppler-silent thrombosis. *J. biomechanical engineering*. (2019).
39. Peskin, C. S. The immersed boundary method. *Acta Numer.* **11**, 479–517 (2002).
40. Sotiropoulos, F. & Borazjani, I. A review of state-of-the-art numerical methods for simulating flow through mechanical heart valves. *Med. & biological engineering & computing* **47**, 245–256 (2009).
41. Hart, J. D., Baaijens, F. P. T., Peters, G. W. M. & Schreurs, P. J. G. A computational fluid-structure interaction analysis of a fiber-reinforced stentless aortic valve. *J. Biomech.* **36**, 699–712 (2003).
42. Loon, R. V., Anderson, P. D. & Vosse, F. N. A fluid structure interaction method with solid rigid contact for heart valve dynamics. *J. Comput. Phys.* **01**, 806–823 (2006).
43. Watton, P. N. *et al.* Dynamic modelling of prosthetic chorded mitral valves using the immersed boundary method. *J. Biomech.* **40**, 613–626 (2007).
44. Luo, X. Y. *et al.* Effect of bending rigidity in a dynamic model of a polyurethane prosthetic mitral valve. *Biomech. Model. Mechanobiol.* **11**, 815–827 (2012).
45. Boffi, D., Gastaldi, L., Heltai, L. & Peskin, C. S. On the hyper-elastic formulation of the immersed boundary method. *Comput. Methods Appl. Mech. Eng.* **197**, 2210–2231 (2008).
46. Griffith, B. E. & Luo, X. Y. Hybrid finite difference/finite element immersed boundary method. *Int. J. for Numer. Methods Biomed. Eng.* **33** (2017).
47. Feng, L. *et al.* On the chordae structure and dynamic behaviour of the mitral valve. *IMA journal of applied mathematics* **83**, 1066–1091 (2018).

48. Yin, M., Luo, X. Y., Wang, T. J. & Watton, P. N. Effects of flow vortex on a chorded mitral valve in the left ventricle. *Int. J. for Numer. Methods Biomed. Eng.* **26**, 381–404 (2010).
49. Meschini, V., Tullio, M. D. D. & Verzicco, R. Effects of mitral chordae tendineae on the flow in the left heart ventricle. *Eur. Phys. J.* **41**, 27 (2018).
50. Casado, J. A. *et al.* Determination of the mechanical properties of normal and calcified human mitral chordae tendineae. *J. Mech. Behav. Biomed. Mater.* **13**, 1–13 (2012).
51. Zuo, K. *et al.* Characterization of biomechanical properties of aged human and ovine mitral valve chordae tendineae. *J. Mech. Behav. Biomed. Mater.* **62**, 607–618 (2016).
52. Ritchie, J., Warnock, J. N. & Yoganathan, A. P. Structural characterization of the chordae tendineae in native porcine mitral valves. *The Annals Thorac. Surg.* **80**, 189–197 (2005).
53. Liao, J. & Vesely, I. A structural basis for the size-related mechanical properties of mitral valve chordae tendineae. *J. Biomech.* **36**, 1125–1133 (2003).
54. Pokutta-Paskaleva, A., Sulejmani, F., DelRocini, M. & Sun, W. Comparative mechanical, morphological, and microstructural characterization of porcine mitral and tricuspid leaflets and chordae tendineae. *Acta Biomaterialia* **85**, 241–252 (2019).
55. Garcia, D. & Kadem, L. What do you mean by aortic valve area: Geometric orifice area, effective orifice area, or gorlin area? *The J. Hear. Valve Dis.* **15**, 601–8 (2006).
56. He, S., Jimenez, J., He, Z. & Yoganathan, A. P. Mitral leaflet geometry perturbations with papillary muscle displacement and annular dilatation: an *in-vitro* study of ischemic mitral regurgitation. *J. Hear. Valve Dis.* **12**, 300 (2003).
57. Sacks, M. S. *et al. In-vivo* dynamic deformation of the mitral valve anterior leaflet. *Annals Thorac. Surg.* **82**, 1369–1377 (2006).
58. Votta, E., Maisano, F., Alfieri, O., Montevecchi, F. M. & Redaelli, A. Finite element models of newly shaped prosthetic rings for the correction of functional mitral regurgitation. *J. Biomech.* **39**, S293–S293 (2006).
59. Votta, E. *et al.* The geoform disease-specific annuloplasty system: A finite element study. *Annals Thorac. Surg.* **84**, 92–101 (2007).
60. Loon, R. V., Anderson, P. D., Vosse, F. N. V. D. & Sherwin, S. J. Comparison of various fluid structure interaction methods for deformable bodies. *Comput. & Structures* **85**, 833–843 (2007).
61. Einstein, D. R., Kunzelman, K. S., Reinhall, P. G., Nicosia, M. A. & Cochran, R. P. The relationship of normal and abnormal microstructural proliferation to the mitral valve closure sound. *J. biomechanical engineering* **127**, 134 (2005).
62. Jimenez, J. H. *et al.* A saddle-shaped annulus reduces systolic strain on the central region of the mitral valve anterior leaflet. *J. Thorac. & Cardiovasc. Surg.* **134**, 1562–1568 (2007).
63. Schoen, F. J. & Levy, R. J. Tissue heart valves: Current challenges and future research perspectives. *J. Biomed. Mater. Res. Part A* **47**, 439–465 (1999).
64. Wang, Q. & Sun, W. Finite element modeling of mitral valve dynamic deformation using patient-specific multi-slices computed tomography scans. *Annals Biomed. Eng.* **41**, 142–153 (2013).

## Acknowledgements

## Author Contributions

L. Cai, and Y. Wang contributed equally to this paper. Y. Wang and R.H. Zhang performed the numerical modelling and wrote the manuscript. L. Cai, H. Gao and X.Y. Luo supervised the overall project. X.S. Ma and G.Y. Zhu provided relevant experimental data. All authors analyzed the results, read and edited the manuscript.

## Additional Information

**Competing Interests:** The authors declare no competing interests.

**Publisher's note:** Springer Nature remains neutral with regard to jurisdictional claims in published maps and institutional affiliations.